

Probing isotopic ratios at $z = 0.89$: molecular line absorption in front of the quasar PKS 1830-211

Muller S.^{1,2}, Guélin M.², Dumke M.^{3,2}, Lucas R.², and Combes F.⁴

¹ Academia Sinica Institute of Astronomy and Astrophysics (ASIAA), P.O. Box 23-141, Taipei, 106 Taiwan

² Institut de RadioAstronomie Millimétrique (IRAM), 300 rue de la piscine, F-38406 St Martin d'Hères, France

³ European Southern Observatory (ESO), Alonso de Cordova 3107, Casilla 19001, Santiago 19, Chile

⁴ Observatoire de Paris, LERMA, 61 av. de l'Observatoire, F-75014 Paris, France

Received 13 March 2006 / Accepted 26 July 2006

ABSTRACT

With the Plateau de Bure interferometer, we have measured the C, N, O and S isotopic abundance ratios in the arm of a spiral galaxy with a redshift of 0.89. The galaxy is seen face-on according to HST images. Its bulge intercepts the line of sight to the radio-loud quasar PKS 1830-211, giving rise at mm wavelengths to two Einstein images located each behind a spiral arm. The arms appear in absorption in the lines of several molecules, giving the opportunity to study the chemical composition of a galaxy only a few Gyr old. The isotopic ratios in this spiral galaxy differ markedly from those observed in the Milky Way. The $^{17}\text{O}/^{18}\text{O}$ and $^{14}\text{N}/^{15}\text{N}$ ratios are low, as one would expect from an object too young to let low mass stars play a major role in the regeneration of the gas.

Key words. Quasars: PKS 1830-211 – Quasars: absorption lines – Astrochemistry – Galaxies: ISM – ISM: molecules, abundances

1. Introduction

The C, N, O, S isotopic abundances are enlightening relics of the interstellar medium (ISM) past history. Not only are these elements the most abundant ones after H and He, but they are those whose synthesis in stars has been the best investigated. The CNO isotopes are tentatively classified into primary elements (^{12}C , ^{16}O , ...), formed directly by He burning, and secondary ones (^{13}C , ^{14}N , ^{17}O , ...) formed at a later stage from primary elements, e.g. through the CNO cycles. In simple evolution models, the fraction of secondary elements increases with time. Actually, chemical evolution is not so straightforward and we know that isotopes like ^{14}N and perhaps ^{13}C are already in part produced in the first generation of stars.

Whereas isotopic abundances can be precisely measured in the Sun and on the Earth, their values in the Galactic ISM and, mostly, in the extragalactic ISM are hard to derive. In a pioneering work, Penzias and co-workers (Penzias et al. 1980, 1981) used the millimeter (mm) emission lines of molecular isotopologues to infer the isotopic ratios in a dozen molecular sources. They found significant differences between the Solar System, the local ISM, the Galactic Center and circumstellar envelopes that they interpreted in terms of degree of nuclear processing, the Solar System representing the state of the local ISM some 4.5 Gyr ago. This picture of the Galactic ISM remains essentially valid today, although it has been recognized that the molecular ratios involving D and ^{13}C are affected by isotopic fractionation or selective photodissociation and may not reflect the elemental isotopic abundance ratios (Wilson & Matteucci 1992).

So far, only a few isotopic abundance ratios have been reported in external galaxies. Those are mostly the C, N, O and S isotopic ratios derived in the nuclei of four nearby starburst galaxies, M 82, IC 342, NGC 253 and NGC 4945, from the mm emission of CO, CS and HCN (Henkel & Mauersberger 1993,

Henkel et al. 1998, Chin et al. 1999, Wang et al. 2004, Martín et al. 2005). These ratios are very uncertain due to beam dilution, because the lines of the rare isotopologues are weak, and because the line opacity of the main isotopologues is unknown. Moreover, the studies deal with nuclear regions that may not reflect the disk ISM abundances, as is the case in the Milky Way.

Another powerful way of studying the composition of the ISM consists in observing the molecular lines in absorption. The method needs only a strong background source and is insensitive to distance and to primary beam dilution. It yields directly the line opacities, provided the background source is fully covered by the intercepting clouds (e.g. Lucas & Liszt 1998). As far as molecular isotopic ratios are concerned, the method is limited to the line of sight to the brightest radio galaxies and quasars intercepted by deep absorption line systems. Few such absorption systems have been identified so far at millimeter wavelengths. They arise in the Milky Way (Lucas & Liszt 1996, 1998) and in a few distant galaxies with redshifts in the range $z = 0.2 - 0.9$ (Wiklind & Combes 1994, 1995, ?, Combes & Wiklind 1998, Combes 1999).

In this article, we present high sensitivity absorption spectra arising from the most remote presently known system, located at $z = 0.89$. The spectra cover the lines of a dozen of molecular species, including the rare isotopomers HC^{17}O^+ , H^{15}NC and C^{34}S . From these spectra, we derive the C, N, O and S isotopic ratios in the spiral arm of a young, seemingly normal galaxy.¹

2. The gravitational lens towards PKS 1830-211

PKS 1830-211 is a radio loud quasar with a redshift of $z = 2.5$ (Lidman et al. 1999), whose line of sight is intercepted by at least two galaxies: a relatively nearby one, responsible for nar-

¹ We adopt the usual convention to simply denote by C, N, O and S the abundant isotopes ^{12}C , ^{14}N , ^{16}O and ^{32}S .

row HI line absorption at redshift $z = 0.19$ (Lovell et al. 1996), and a more distant one that gives rise to broad molecular and HI line absorption at $z = 0.89$ (Wiklind & Combes 1996 and 1998, hereafter WC96 & WC98, Gérin et al. 1997, Menten et al. 1999, Chengalur et al. 1999, Muller & Guélin 2003). No molecular absorption is detected in the first galaxy (WC98) while the latter galaxy acts as a gravitational lens and gives rise, at radio wavelengths, to two compact sources (NE and SW) embedded in a faint Einstein ring (see Fig.3 from Chengalur et al. 1999, see also Jauncey et al. 1991). The ring has a steep spectral index and fades away at short wavelengths (Carilli et al. 1998), so that at mm wavelengths, the quasar image reduces essentially to the NE and SW sources that are distant by $\approx 1''$, plus two weak 'tails' (Frye et al. 1997, WC98, Carilli et al. 1998).

The $z = 0.89$ absorption system shows two main velocity components: a broad one at $z = 0.88582$ (assuming $V = 0 \text{ km s}^{-1}$ in heliocentric coordinates), associated with the SW source, and a narrow component, 147 km s^{-1} lower in velocity, associated with the NE source (Frye et al. 1997, WC98). Although both components are detected in absorption in HI and in molecular lines, the NE component is more conspicuous in the HI line and the SW one in the molecular lines (WC98, Chengalur et al. 1999).

Recently, Winn et al. (2002) have published a HST I-band image of the $z = 0.89$ lensing galaxy. This latter appears as a typical nearly face-on spiral (probably of type Sb or Sc). The low inclination of the galaxy is confirmed by Koopmans & de Bruyn (2005), who modelled its kinematics from the HI absorption profile and find $i = 17^\circ - 32^\circ$. The bulge of the galaxy is located near the center of the radio ring. The SW radio source appears to lie right on top of a spiral arm, at a (model dependent) distance of $\approx 2 \text{ kpc}$ from the center. The NE source lies at about twice this distance ($\approx 4 \text{ kpc}$) on the other side of the nucleus. Both absorption components seem thus to arise in the counterpart of what we call in the Milky Way the Molecular Ring.

Adopting the cosmological parameters $H_0 = 70 \text{ km s}^{-1} \text{ Mpc}^{-1}$, $\Omega_M = 0.3$ and $\Omega_\Lambda = 0.7$, the redshift $z = 0.89$ corresponds to a lookback time of 7.2 Gyr, yielding an age $\leq 6 \text{ Gyr}$ for the galaxy. Assuming that the first generation of stars formed 1 Gyr after the Big Bang, stars with masses $< 1.5 M_\odot$ barely had the time to contribute to the enrichment of the interstellar medium.

3. Observations

With the Plateau de Bure Interferometer (PdBI), we have carried out a high sensitivity and high spectral resolution survey of a dozen of mm absorption lines in the line of sight to PKS 1830-211. This survey is the result of a number of 2 – 4 hour-long observing sessions, carried out between 1999 and 2005 (see Table 2). The antennas were most of the time in a compact configuration which led to a synthesized beam $\sim 10''$ at $\nu = 100 \text{ GHz}$ ($\delta = -21^\circ$), much larger than the source size. The phase reference was set at R.A. = $18^{\text{h}}33^{\text{m}}39^{\text{s}}.937$, Dec. = $-21^\circ03'39''.80$ (J2000). The spectral resolution was 1.25 MHz before 2000, and 2 or 4 times better afterwards. For calibration purpose, a strong continuum source (usually 3C273 or 3C345), free of any absorption at the frequencies of interest was observed for 10 minutes shortly before and after PKS 1830-211.

The data were reduced and analyzed with the GILDAS/CLIC software. The data from each observing session were first calibrated for instrumental RF bandpass by fitting a high order polynomial on the spectrum observed for the strong continuum

Table 1. Basic data for PKS 1830-211 and the intervening galaxy.

PKS 1830-211			
NE image	R.A. (J2000)	$18^{\text{h}}33^{\text{m}}39^{\text{s}}.932$	(1)
	Dec. (J2000)	$-21^\circ03'39''.73$	(1)
SW image	R.A. (J2000)	$18^{\text{h}}33^{\text{m}}39^{\text{s}}.886$	(1)
	Dec. (J2000)	$-21^\circ03'40''.45$	(1)
Redshift		$z = 2.5$	(2)
3mm flux density	(variable)	$1.5 - 2.5 \text{ Jy}$	
Flux distribution	NE image	$\sim 63\%$	(3)
	SW image	$\sim 37\%$	(3)
Intervening galaxy			
Redshift		$z = 0.88582$	(3)
Type		Sb or Sc	(4)
Inclination		$17^\circ - 32^\circ$	(5)
Linear scale		$1'' \sim 7.8 \text{ kpc}$	
Velocity	SW absorption	$\sim 0 \text{ km s}^{-1}$	(6)
	NE absorption	$\sim -147 \text{ km s}^{-1}$	(6)
Age		$\leq 6 \text{ Gyr}$	

References: (1) Subrahmanyan et al. 1990; (2) Lidman et al. 1999; (3) WC96; (4) Winn et al. 2002; (5) Koopmans & de Bruyn (2005); (6) WC98.

source. We checked that this calibration was accurate to better than 1%.

Next, the spectral data were calibrated in amplitude and phase with respect to the PKS 1830-211 continuum, whose flux was $\approx 2 \text{ Jy}$ at $\lambda = 3 \text{ mm}$. PKS 1830-211 being unresolved in the compact antenna configurations, the phases in this process were referenced to the barycenter of the continuum emission and the amplitudes normalized to the total continuum flux. Finally, the spectra observed on the different sessions and with the different baselines were co-added and a third-degree baseline withdrawn from the global spectrum, in order to remove small RF bandpass residuals (amplitude $\sim 2\%$) caused by instrumental drifts and/or strong atmospheric fluctuations.

The total integration time per line ranges from 1 h to 20 h; the rms noise on the weakest lines is between 2 and 7 mJy per 1.25 MHz channel.

In addition to the compact configuration observations just described, and which served as the basis of our molecular line survey, we observed on 2003 February 26th and March 1st the HCO⁺ ($2 \leftarrow 1$) line in the extended A configuration. This configuration includes 400 m-long E-W and NE-W baselines that allow to spatially resolve the NW and SW source components. We used a special procedure to reduce these data. This procedure is described in §4.1.

Finally, we also observed on 2003 August 3rd the ($2 \leftarrow 1$) line of HCN with the IRAM 30-m telescope. The spectrum shown in Fig. 3 is the sum of the 30-m and PdBI data.

4. Data analysis

4.1. Position of the absorptions

Using the BIMA array, Frye et al. 1997 (see also Swift et al. 2001) successfully resolved the two continuum components. They derived an angular separation of $0.99'' \pm 0.05''$. Further evidence that the NE component was indeed responsible for the second absorption at $V = -147 \text{ km s}^{-1}$ was shown by WC98. They used the BC configuration of the PdBI and fitted the position of the barycenter of emission directly from the visibilities.

Our A configuration PdBI observations of the HCO^+ ($2 \leftarrow 1$) line, which combine high sensitivity and high angular resolution enable us to locate with a much higher relative accuracy the velocity components. For this, we used the following procedure.

The RF bandpass was first calibrated using the quasar 1749+096 (on 2003 Feb. 26^h) or 3C273 (on 2003 Mar. 1st). Next, the continuum data on PKS 1830-211 were self-calibrated by calculating the complex gains (amplitude and phase) corresponding to a point-like source of flux unity at the phase center. The latter was fixed through this procedure at the barycenter of the continuum emission. Then, the calculated gains were applied to the line visibilities and the continuum was subtracted. The resulting visibilities were fitted by a point source, channel by channel, to trace the position of the absorption. At this step, the absorptions at $V \approx -147 \text{ km s}^{-1}$ and $V \approx 0 \text{ km s}^{-1}$ were already clearly found to arise from two different locations (NE and SW respectively) separated by $1.01'' \pm 0.03''$ at a position angle of $\sim 42^\circ$.

The whole process was iterated: *i*) A new input continuum model, consisting of two point-like sources, located at the previously derived NE and SW positions and with fluxes in the ratio 1.7 (see Table 3), was used to self-calibrate the data. *ii*) the new continuum was subtracted from the calibrated visibilities to yield the amplitude of the absorption and its position in each velocity channel (Fig. 1).

We confirm that the two main absorption components (around $V = 0 \text{ km s}^{-1}$ and $V = -147 \text{ km s}^{-1}$) arise from two distinct compact sources, whose relative positions, estimated from weighted averages over each component, are $(0.420'' \pm 0.008''; 0.45'' \pm 0.03'')$ for the NE component and $(-0.255'' \pm 0.002''; -0.279'' \pm 0.006'')$ for the SW component. This corresponds to a separation of $0.99'' \pm 0.03''$ and a position angle of $43^\circ \pm 1^\circ$, in good agreement with the separation and position angle of the continuum sources derived from BIMA, MERLIN and VLA observations.

One purpose of our extended configuration observations was to check whether the 80 km s^{-1} -broad absorption component centred at 0 km s^{-1} was arising entirely from the compact SW image, or if the line shoulders and/or wings were arising from the dimmer ‘tails’ and ‘knots’ visible at longer wavelengths, or from the weak Einstein ring. It should be noted that the $V = 0 \text{ km s}^{-1}$ HCO^+ and HCN absorption profiles observed at 3-mm at low angular resolution are almost twice broader than those observed at 6-mm with a $0.1''$ resolution (Carilli et al. 1998).

Fig. 1 shows that the absorption arises within $0.1''$ ($0.2''$ in weak wings of the line) from a point-like source and shows no obvious velocity/position gradient. In particular, the emission at $V < -20 \text{ km s}^{-1}$ and $V > 20 \text{ km s}^{-1}$, which is not observed in the high resolution VLA and VLBA observations, does not arise from the ‘tails’ and ‘knots’, but comes from the compact SW ‘core’.

4.2. Magnification ratio

The flux of PKS 1830-211 is known to be variable. For example, van Ommen et al. (1995) report a variation of the 15 GHz flux by a factor of 2 between 1990 and 1991, whereas Wiklind & Combes (1999) observe a similar increase of the 3-mm flux between 1997 and 1998. Although the 3-mm flux was mostly stable and close to 2.5 Jy in the course of our survey, we noted 20 – 30% changes between 1999 and 2001 and between 2001 and 2002. There was no significant change around August 2002, the period when the HNC line was observed.

A question central to this study is whether the magnification ratio of the NE and SW sources, $\mathfrak{R} = \text{NE/SW}$, is also variable, as this would affect the amplitude of the $V = 0$ and -147 km s^{-1} absorption components with respect to the continuum flux. \mathfrak{R} is expected to vary after a sudden increase of the flux of the background quasar, since the increase will first appear in the NE source, then in the SW source after a delay $\Delta\tau$. The path length from the quasar to the observer is indeed shorter for the rays passing through the NE source (Nair et al. 1993). $\Delta\tau$ has been measured by Lovell et al. (1998) and by Wiklind & Combes (1999) and found to be about 25 days. Micro-lensing events caused e.g. by stars may also randomly affect \mathfrak{R} for short periods of time.

In order to check for variations of \mathfrak{R} during the period of our observations, we have regularly observed the absorption spectrum of the HCO^+ ($2 \leftarrow 1$) line. Fig. 2 shows the line profiles on 4 different epochs. We see no variations in the lineshape or absorption depth that exceeds the 1-sigma rms uncertainty (typically a few percent – see Table 3). The 0 km s^{-1} component is known to be saturated in the HCO^+ line. Assuming all the emission near 0 km s^{-1} comes from the NE source, we derive relative intensities of 37% and 63% for the SW and NE continuum sources, and a magnification ratio $\mathfrak{R} = 1.66$ (Table 3). The lack of obvious variations of \mathfrak{R} during our observing period simply means that the flux variations over intervals of time of 25 days were either small, or constant.

During their 3-year long monitoring of the HCO^+ ($2 \leftarrow 1$) line with the 30-m telescope (1996 – 98) Wiklind and Combes also observed magnification ratios in the range 1.4 – 1.7 with only a few excursions to values differing from $\mathfrak{R} = 1.6$ by more than 2σ (1σ was typically 0.1). Swift et al. (2001) reported a significantly smaller ratio (1.2) for Dec. 1999, but this low ratio comes from the separation of the two continuum sources in a half-resolved map. Our average ratio is close to that measured with the VLA at 15 GHz and 23 GHz by Nair et al. (1993) in 1987 – 1990 (1.5 – 1.6).

We therefore assumed in the following that the relative fluxes of the NE and SW sources remained constant during our observations and simply co-added, when necessary, the calibrated spectra observed on different sessions. A variation of \mathfrak{R} (e.g. by 20%) for short periods of time is however not excluded: it would merely change the absorption depths measured on those short periods (by $\approx 13\%$). This would have no significant effect on most isotopic ratios, that average data of different observing periods (see Table 2).

4.3. Absorption profiles and opacities

Fig. 3 presents the absorption profiles for the ($J=2 \leftarrow 1$) lines of HCO^+ , HCN and HNC. Both the $V = 0 \text{ km s}^{-1}$ and $V = -147 \text{ km s}^{-1}$ components are detected in these 3 lines. The $V = -147 \text{ km s}^{-1}$ component had been previously observed by WC98, but only for the HCO^+ line and with a lower signal to noise ratio.

The absorption profiles of the $V = 0 \text{ km s}^{-1}$ and $V = -147 \text{ km s}^{-1}$ components are not Gaussian. The HNC ($2 \leftarrow 1$) $V = 0 \text{ km s}^{-1}$ component consists of at least 3 Gaussian sub-components (Fig. 5) and the $V = -147 \text{ km s}^{-1}$ component of 2 sub-components, which implies the presence of several clouds in front of the SW and NE sources. The 5 Gaussian sub-components have velocities of $\approx -155, -150, -21, -3$ and $+7 \text{ km s}^{-1}$. Their widths ($\approx 10 - 20 \text{ km s}^{-1}$) are typical of the width of Milky Way Giant Molecular Clouds.

A comparison of the HNC, HCN and HCO^+ line profiles suggests a similar set of clouds with similar relative abundances,

Table 3. Measurements of the magnification factors.

Epoch	NE/SW ratio
1995 Sep. 29 †	1.6 ± 0.2
1995 Sep. 30 †	1.6 ± 0.2
1995 Oct. 01 †	1.5 ± 0.1
1995 Oct. 26 †	1.8 ± 0.2
1999 Jun. 11	1.65 ± 0.02
2001 Mar. 20	1.55 ± 0.04
2001 Jun. 29	1.65 ± 0.02
2002 Jun. 25	1.68 ± 0.05
2003 Feb. 26	1.66 ± 0.07
2003 Mar. 01	1.75 ± 0.07

Notes: The magnification factor (NE/SW) is determined with the PdBI from the saturation level of the HCO^+ ($2 \leftarrow 1$) line absorption at $V \approx 0 \text{ km s}^{-1}$. In the case of extended configuration, baselines longer than 300 m were flagged out.

† Re-reduction of previous PdBI observations (WC98).

but with an increasing opacity from HNC to HCO^+ . A modelling of the line opacities, assuming that the SW source contains 37% of the total continuum flux, as derived in §3, and that the source filling factor by the absorbing clouds is close to 1, yields an opacity $\tau \approx 2$ at the peak of the HNC line, and a HCN/HNC opacity ratio of ≈ 3 , fairly constant across the entire spectrum, from -160 to $+20 \text{ km s}^{-1}$.

Fig. 4 shows the $J=2 \leftarrow 1$ line profiles of the rare ^{13}C , ^{15}N , ^{17}O and ^{18}O isotopologues of HCO^+ , HCN and HNC, as well as those of CS and C^{34}S $J=4 \leftarrow 3$, and H_2S and H_2^{34}S ($J_{K_1, K_2} = 1_{10} \leftarrow 1_{01}$). For these species, only the SW absorption is detected. The profiles of HNC and of the rare isotopomers are not flat-topped, but show narrow peaks near 0 km s^{-1} . They are not only sharper than those of the main HCO^+ and HCN isotopomers, but also shallower, indicating that they are not saturated. The absorption lines of H^{13}CO^+ , HC^{18}O^+ , H^{13}CN and HC^{15}N show very similar profiles, while the spectra of CS and H_2S look different: the $+7 \text{ km s}^{-1}$ sub-component is much enhanced for those species. The similarity of the line opacity profiles of H^{13}CO^+ and HNC is illustrated in Fig. 5.

Assuming, again, that the SW source represents 37% of the total flux and that its filling factor is unity, the line opacity $\tau(v)$ is given by:

$$\tau_{app}(v) = -\ln\left(\frac{I(v) - I_{sat}}{|I_{sat}|}\right) \quad (1)$$

where $I(v)$ is the depth of the absorption from the continuum level and I_{sat} the saturation level: $I_{sat}^{SW} = -37\%$ and $I_{sat}^{NE} = -63\%$ (we assume that the contribution from the Einstein ring is negligible at mm wavelengths). We emphasize here that the knowledge of the relative fluxes of the components allows us to derive the optical depths without any assumption on the line excitation temperature other than it is small with respect to the temperature of the quasar image. The major source of uncertainty on τ is coming from the filling factor, that may vary with velocity and species. However, we expect that all the isotopologues have the same spatial distribution, hence the same filling factor, as the abundant ones.

The flat shape of the HCO^+ and HCN profiles around 0 km s^{-1} suggests that the clouds cover entirely the SW source. This coverage, however, may not be uniform, as the SW source size ($\geq 2.5 \text{ mas}$, Carilli et al. 1998) is $\geq 10 \text{ pc}$ at the distance of the galaxy and presumably large with respect to individual

clouds. The apparent opacities in equation [1] are thus strictly speaking lower limits to the true opacities. However, the similarity of the absorption profiles on Fig. 4, which yet have very different opacities, suggests that the true opacities are not large, except for HCO^+ and HCN near 0 km s^{-1} , and that the values derived from equation [1] are close to the true opacities. This is illustrated in Fig. 5 which shows the opacity profiles of the HNC, H^{13}CO^+ and HC^{18}O^+ ($2 \leftarrow 1$) lines, all of which are indeed very similar. We note that Carilli et al. (1998) measure for the HCN ($1 \leftarrow 0$) line an integrated apparent opacity $\int \tau dV = 0.7 \text{ km s}^{-1}$ for the NE ($V = -147 \text{ km s}^{-1}$) component that agrees fairly well with our value of 3.5 km s^{-1} for the ($2 \leftarrow 1$) line, demonstrating that the component is indeed optically thin.

We have fitted the opacity profiles (eg. Fig. 5) derived with equation [1] for all the observed species with 4 Gaussian components: 3 for the SW source ($-50 \leq V \leq +40 \text{ km s}^{-1}$), and one for the NE source ($-160 \leq V \leq -140 \text{ km s}^{-1}$), which is too weak to be resolved, except in the HCO^+ line. The fitted parameters (sub-component velocities, peak opacities and velocity widths) and integrated opacities are listed in Table 4 and Table 5 for the SW and NE components, respectively. The mean central velocities of the 3 absorption components towards SW are -21 , -3 and 7 km s^{-1} , and their mean linewidths are 13 , 8 and 10 km s^{-1} . The linewidths of these different components are typical of Giant Molecular Clouds in the Milky Way Molecular Ring.

Note that we could not derive reliable parameters for the rare isotopomer HC^{15}N because of low S/N, and fixed the velocities of 2 Gaussian profiles to -3 and 7 km s^{-1} . For the same reason, the NE absorption of the CS spectrum was fitted with velocity and width fixed to the same values as the HCN NE fit.

Table 5. Fit of the NE opacity profiles.

Line	V_0 (km s^{-1})	τ	$\Delta V_{1/2}$ (km s^{-1})	$\int \tau dV$ (km s^{-1})
HCO^+ (1-2)	-147.2	0.35	14.7	5.5 (0.05)
HCN (1-2)	-146.4	0.28	11.6	3.5 (0.2)
HNC (1-2)	-146.0	0.07	14.1	1.1 (0.05)
CS (3-4)	-146.4 †	0.02	11.6 †	0.28 (0.08)
H^{13}CO^+ (1-2)	-	(0.007)	14.7 †	≤ 0.12

Notes: Uncertainties and upper limits on the integrated opacities are calculated as mentioned in the caption of Table 4.

† Fixed parameter.

5. Isotopic ratios

In order to derive the line opacity ratios and the column density ratios of the different isotopologues, we assume that all the isotopologues from a same molecular species have the same spatial distribution and are similarly excited, hence that their line opacity profiles are similar.

The first hypothesis should be fulfilled, except for the species deeply affected by isotopic fractionation. In cold Galactic clouds, the abundances of molecules bearing ^{13}C and, mostly, D atoms are known to be significantly affected by fractionation reactions and selective photodissociation. This is not the case, however, for the other species (see e.g. Langer et al. 1984), and we will assume that their relative abundances do reflect the elemental isotopic abundance ratios. The hypothesis of similar spatial distribution is not critical in the sense that it yields isotopic

ratios averaged over the (small) continuum source, as long as the line is not too optically thick.

The hypothesis of similar excitation is certainly correct for most line components and species: all the species studied here have large dipole moments and are hard to excite. Since the bulk of the absorption caused by a cloud > 10 pc with $N(\text{H}_2) = \text{few} \times 10^{22} \text{ cm}^{-2}$ (Menten et al. 1999) is likely to arise in a low density envelope ($n \leq \text{few} \times 10^2 \text{ cm}^{-3}$), the molecules are essentially heated by the 5.1 K cosmic background, so that $T_{\text{rot}} \approx 5.1$ K. The lines of the main HCO^+ and HCN isotopologues, the opacity of which is large between -10 and $+10 \text{ km s}^{-1}$, were not considered inside this velocity range for the derivation of the isotopic ratios.

The line opacity ratios derived for the different pairs of isotopologues are shown in Table 6. These ratios were calculated in the following way: five line opacity profiles, assumed to be identical for all isotopologues of a given molecular species, were derived by fitting the line opacity profiles of H^{13}CO^+ , H^{13}CN , HNC, CS and H_2S with Gaussian components, as explained in §4.3 (see Fig. 5 and Table 4). Those species were selected because they are observed with a good signal-to-noise ratio and have a low or moderate opacity. The fitted opacity profiles were then sampled at the velocity resolution of the observations and squared to yield weights. The rare-to-abundant isotope line opacity ratio was then calculated as the weighted average \bar{R} of the ratios measured for each velocity channel, in the velocity ranges $-10 < V < 10 \text{ km s}^{-1}$ (line center) or $-40 < V < -10 \text{ km s}^{-1}$ (line wing). Finally, \bar{R} was inverted to yield the abundant-to-rare line opacity ratio, \bar{R}^{-1} .

Similarly, the uncertainties on the line opacity ratios were first estimated for the rare-to-abundant ratios, R . In all cases, the uncertainties are dominated by the noise on the rare isotopologue. Then, R can be roughly described as a normal variable of variance σ^2 . The error bars on the inverse (abundant-to-rare) ratio \bar{R}^{-1} were then derived as equal to $-(\bar{R}^{-1} - (\bar{R} + \sigma)^{-1})$ and $+(\bar{R} - \sigma)^{-1} - \bar{R}^{-1}$. Note that the bars are asymmetric for low signal-to-noise ratios. A more accurate evaluation of the errors from the likelihood function yields identical results.

Within our hypothesis of similar spatial distribution and similar excitation, the values of Table 6, multiplied by the inverse ratio of the square of the line frequencies, reflect the molecular isotopic abundance ratios.

We note that the $^{12}\text{C}/^{13}\text{C}$ and $^{14}\text{N}/^{15}\text{N}$ ratios derived from different species (e.g. HCN and HNC) and velocity components (e.g. wings vs center of line) agree within the quoted uncertainties. We come back to this point when we discuss the elemental isotopic ratios individually.

The elemental isotopic ratios derived by averaging² the values of Table 6 are given in Table 7, where we list, for comparison, the isotopic ratios in a number of Galactic and extragalactic sources. The former are the Solar System (SS), whose isotopic ratios probably represent the state of the ISM 4.5 Gyr ago, the local ISM, the Galactic Center (GC), which can be considered at a later stage of evolution, and the carbon rich circumstellar envelope IRC+10216 that consists of material entirely reprocessed in the core of a $\approx 2 M_{\odot}$ AGB star. The latter are giant clouds from the Large Magellanic Cloud (LMC), that are characterized by a low metallicity, and the nuclear regions of two nearby starburst galaxies, NGC 253 and NGC 4945.

The local ISM values come from Lucas & Liszt (1998) and were derived through absorption measurements against extra-

Table 6. Line opacity ratios derived from our observations with the IRAM interferometer.

Lines	Velocity interval	Line opacity ratios
$\text{HCO}^+ / \text{H}^{13}\text{CO}^+ (2 \leftarrow 1)$	SW wings	28 (3)
$\text{HCN} / \text{H}^{13}\text{CN} (2 \leftarrow 1)$	SW wings	40 (-5+7)
$\text{HNC} / \text{HN}^{13}\text{C} (2 \leftarrow 1)$	SW	27 (3)
$\text{H}^{13}\text{CN} / \text{HC}^{15}\text{N} (2 \leftarrow 1)$	SW	4.2 (0.3)
$\text{HN}^{13}\text{C} / \text{H}^{15}\text{NC} (2 \leftarrow 1)$	SW	6 (-2+4)
$\text{HNC} / \text{H}^{15}\text{NC} (2 \leftarrow 1)$	SW	166 (-58+194)
$\text{HCO}^+ / \text{HC}^{18}\text{O}^+ (2 \leftarrow 1)$	SW wings	53 (-10+16)
$\text{H}^{13}\text{CO}^+ / \text{HC}^{18}\text{O}^+ (2 \leftarrow 1)$	SW	2.01 (0.07)
$\text{HC}^{18}\text{O}^+ / \text{HC}^{17}\text{O}^+ (2 \leftarrow 1)$	SW	12 (-2+3)
$\text{CS} / \text{C}^{34}\text{S} (4 \leftarrow 3)$	SW	10.4 (-0.7+0.8)
$\text{H}_2\text{S} / \text{H}_2^{34}\text{S} (1_{10} \leftarrow 1_{01})$	SW	8 (1.5)

Notes: The SW component corresponds to velocities in the range -10 to $+10 \text{ km s}^{-1}$ and the SW wings to -40 to -10 km s^{-1} . The quoted errors, 1σ , reflect the noise and baseline uncertainties, but not the uncertainties on the magnification ratio \mathfrak{R} , which is assumed to remain constant.

galactic continuum sources. They probably refer to the same type of clouds as those observed in our remote galaxy and are the most accurate values of Table 7. The envelope IRC+10216 is probably typical of the matter recycled to the ISM by low-mass stars. It is thought that two-third of the matter presently ejected by the stars in the Galactic ISM comes from such low mass stars. The sequence SS-ISM-GC-IRC+10216 may thus be considered in the first approximation as one of increasing processing of the gas by low-mass stars.

5.1. Carbon

The $^{12}\text{C}/^{13}\text{C}$ elemental isotopic ratio is difficult to measure, since the main ^{12}C isotopologues tend to be saturated when its ^{13}C counterpart becomes detectable. This ratio, on the other hand, can be derived in our survey from 3 different molecules: HCO^+ , HCN and HNC. H^{13}CO^+ , H^{13}CN and HN^{13}C are all detected in the SW component ($V = -3 \text{ km s}^{-1}$ component), but both HCO^+ and HCN are heavily saturated at the peak of the line. The $^{12}\text{C}/^{13}\text{C}$ ratio can thus be measured only in the line wings ($V < -10$ and $V > 10 \text{ km s}^{-1}$). The opacity of the HNC line (≤ 2 , see Fig. 5) is low enough to allow an estimate of the $^{12}\text{C}/^{13}\text{C}$ ratio even at the center of the line. Within the uncertainties, we find the same ratio for the 3 molecular species: ≈ 30 . The mean isotopic ratio, estimated from a weighted average of the HCO^+ , HCN and HNC line opacity ratios, is 27 ± 2 , where the uncertainty only reflects the noise and the calibration errors, but not residual opacity effects linked e.g. to a change in the magnification ratio. Considering these restrictions, our ratio is in good agreement with that derived by Menten et al. (1999) from VLA HNC ($J = 1 \leftarrow 0$) line observations for the same velocity component: ≈ 35 . The $J = 1 \leftarrow 0$ HNC line is less optically thick than the $J = 2 \leftarrow 1$ line, but the VLA HN^{13}C spectrum has a lower velocity resolution and is noisier than our spectra.

The relative abundances of ^{12}C and ^{13}C can be affected by isotopic fractionation (Lucas & Liszt 1998). Milam et al. (2005), however, argue that the effects are limited and should not affect the isotopic ratios at the scales involved here. The agreement between the ratios derived from three different species and from two lines of the same species gives us confidence

² The mean value of the R_i, σ_i estimations was calculated as $\bar{R} = (\sum R_i / \sigma_i^2) / (\sum 1 / \sigma_i^2)$ with a variance $\sigma^2 = 1 / (\sum 1 / \sigma_i^2)$.

that the $^{12}\text{C}/^{13}\text{C}$ ratio in the SW source is indeed close to 27. Unfortunately, none of the ^{13}C species is detected in the NE component ($V = -147 \text{ km s}^{-1}$). The upper limit on H^{13}CO^+ yields a 3σ lower limit to the $\text{HCO}^+/\text{H}^{13}\text{CO}^+$ ratio of 31, similar to the value of this ratio in the SW component.

The interpretation of the $^{12}\text{C}/^{13}\text{C}$ ratio in terms of nucleosynthesis is also not straightforward. ^{12}C is a primary product of helium burning in intermediate and massive stars. ^{13}C forms from ^{12}C through the CNO cycles in the H-burning shell. It may form in H-burning shell of the very massive stars that produce ^{12}C and/or could be produced later in a second generation of intermediate or low mass stars (Prantzos et al. 1996). In the later scheme, the abundance of ^{13}C relative to ^{12}C is expected to increase with time and the degree of processing of the gas, but the observed $^{12}\text{C}/^{13}\text{C}$ ratio is not significantly lower in the IRC+10216 envelope than in the local interstellar medium (45 vs 59, see Table 7) which suggests that ^{13}C behaves at least partly as a primary element. Thus, the low value of the $^{12}\text{C}/^{13}\text{C}$ ratio in the $z = 0.89$ galaxy may not be very meaningful.

5.2. Nitrogen

A direct measurement of the $^{14}\text{N}/^{15}\text{N}$ ratio is even more difficult than for the $^{12}\text{C}/^{13}\text{C}$ ratio, as it is larger. We derive this ratio directly from HNC for the $V = -3 \text{ km s}^{-1}$ component, or indirectly from the double $(\text{H}^{13}\text{CN}/\text{HC}^{15}\text{N}) \times [^{12}\text{C}/^{13}\text{C}]$ ratio. The isotopic ratios we arrive at are consistent and yield an average ratio $^{14}\text{N}/^{15}\text{N} = 130 \pm 20$, a factor of two smaller than its Solar System and local ISM values.

The relative abundances of ^{14}N and ^{15}N are strongly affected by nuclear processing. In low mass stars, where the temperature of the H-burning zone is $\leq 10^8 \text{ K}$, the cold CNO cycles convert essentially C, N and O into ^{14}N and destroy most of ^{15}N . In massive stars, ^{15}N is produced at equilibrium through the hot CNO cycle. In explosive episodes that mark the end of those stars (novae and supernovae), ^{14}N is quickly converted into ^{15}N and ^{18}O . As a result, the $^{14}\text{N}/^{15}\text{N}$ ratio is a sensitive probe of the type of stars governing the nucleosynthesis; it should increase with the degree of processing by low mass stars. Indeed, $^{14}\text{N}/^{15}\text{N}$ is found to be much larger in the Galactic Center region than in the local ISM or in the Solar System and reaches an even larger value in the circumstellar shell IRC+10216 (Table 7). In contrast, the low ratio measured toward PKS 1830-211 fits well with the scenario where low mass stars played almost no role in the composition of the ISM in the $z = 0.89$ galaxy.

5.3. Oxygen

Because its value is very large, the $^{16}\text{O}/^{18}\text{O}$ ratio is usually measured through the double $[^{13}\text{C}/^{12}\text{C}] \times [^{16}\text{O}/^{18}\text{O}]$ ratio. The value we derive in this way, ≈ 60 , is very low compared to the Solar and interstellar values (≈ 600), even though allowance should be made for a possible underestimation of $^{12}\text{C}/^{13}\text{C}$, due to fractionation or residual opacity effects. That the actual ratio is low is confirmed by our direct measurement of the $\text{H}^{12}\text{C}^{16}\text{O}^+/\text{H}^{12}\text{C}^{18}\text{O}^+$ ratio in the wings of the SW component (Table 6), which also yields ≈ 60 . This result is surprising, since both ^{16}O and ^{18}O form in massive stars and are predicted to behave about similarly, except at early ages, since ^{16}O is a primary element and ^{18}O a secondary element. And indeed, the $^{16}\text{O}/^{18}\text{O}$ ratio is found to decrease mildly or not at all between the local ISM to the Galactic Center (see Table 7 and Polehampton et al. 2005). At early ages, the $^{16}\text{O}/^{18}\text{O}$ ratio is supposed to be larger (Prantzos

et al. 1996). The $^{16}\text{O}/^{18}\text{O}$ ratio in the Solar System, 1.6 times smaller than in the ISM, is however a well known puzzle in this context and is sometimes interpreted by an overabundance of ^{16}O in the Solar Nebula.

The $^{18}\text{O}/^{17}\text{O}$ ratio, which is small and stems from lines that are certainly optically thin, may be more accurately derived. According to the current nucleosynthesis models, the $^{16}\text{O}/^{18}\text{O}$ and $^{16}\text{O}/^{17}\text{O}$ isotopic ratios are sensitive indicators of the stellar mass, ^{18}O being essentially formed and released by short-lived massive stars while ^{17}O comes mostly from long-lived low-mass stars (see e.g. Landré et al. 1990, Prantzos et al. 1996). Our ratio $^{18}\text{O}/^{17}\text{O} = 12$ is very large, compared to the canonical ISM value of 3 – 4 (Penzias 1981, Bensch et al. 2001, Wouterloot et al. 2005) and to the Solar System value of 5.5. It is especially large with respect to the value observed in IRC+10216 and in other late type giant envelopes which are all < 1 (Kahane et al. 1992).

The high $^{18}\text{O}/^{17}\text{O}$ and low $^{16}\text{O}/^{18}\text{O}$ ratios, compared to the ISM and, mostly, to IRC+10216, are probably linked to the relative youth of the $z = 0.89$ galaxy. They may help us to better understand the puzzling ^{18}O nucleosynthesis. It is worth noting that Combes & Wiklind (1995) derived from similar absorption observations a limit $\text{C}^{18}\text{O}/\text{C}^{17}\text{O} > 15$ in another high redshift galaxy ($z = 0.68$) on the line of sight to the quasar B0218+357.

The $^{18}\text{O}/^{17}\text{O}$ ratio has been estimated in the starburst nuclei of M 82, NGC 253 and NGC 4935 (Sage et al. 1991, Henkel & Mauersberger 1993). The values, which are much more uncertain than in the cases of the ISM and the $z = 0.89$ galaxy, seem larger than the Local ISM value and may be explained by a initial mass function biased towards massive stars (Henkel & Mauersberger 1993).

Fig. 7 compares in a single diagram the relative abundances of ^{16}O , ^{17}O and ^{18}O as observed for the main Galactic and extragalactic sources. ^{17}O appears particularly abundant in IRC+10216 and ^{16}O unabundant in the $z = 0.89$ galaxy. The LMC stands in this diagram at the opposite of the $z = 0.89$ galaxy, but this could be an artifact of low metallicity and strong UV radiation field, which may lead to selective photodissociation of the rare C^{18}O and C^{17}O isotopes.

5.4. Sulfur

The $^{32}\text{S}/^{34}\text{S}$ ratio we derive from CS and H_2S , 10 ± 1 , is at the same time accurate, since it is directly measured on optically thin lines for two different species, and meaningful, since only few molecular sources show such a clear departure of this ratio from its Solar System value, 22.

The $^{32}\text{S}/^{34}\text{S}$ ratio is found to be the same in the processed stellar envelope IRC+10216, in the Solar System and in the local ISM. The $^{34}\text{CS}/^{33}\text{CS}$ ratio is the same in all Galactic molecular sources, and the $^{13}\text{CS}/\text{C}^{34}\text{S}$ ratio, which is used to estimate the $^{32}\text{S}/^{34}\text{S}$ ratio in Giant Molecular Clouds where ^{12}CS is optically thick, shows no variations across the Galaxy (Frerking et al. 1980, Chin et al. 1996).

Because the $^{12}\text{C}/^{13}\text{C}$ ratio derived from H_2CO and CO seems to decrease between the Solar neighbourhood and the Galactic Center, Chin et al. (1996) argue that the constancy of $^{13}\text{CS}/\text{C}^{34}\text{S}$ implies a similar decrease of $^{32}\text{S}/^{34}\text{S}$. The $^{12}\text{C}/^{13}\text{C}$ gradient, however, is shallow, except perhaps near the Galactic Center. Moreover, CO and H_2CO yield for the same galactocentric radius discrepant values (Wilson & Rood 1994). Thus, the observed $^{12}\text{CO}/^{13}\text{CO}$ and $\text{H}_2^{12}\text{CO}/\text{H}_2^{13}\text{CO}$ ratios may well be affected by ^{13}C fractionation and/or line opacity effects and may

not reflect the $^{12}\text{CS}/^{13}\text{CS}$ ratio, so that the presence of a $^{32}\text{S}/^{34}\text{S}$ gradient in the Galaxy is not established. As a matter of fact, it would be quite surprising to find a low $^{32}\text{S}/^{34}\text{S}$ ratio in the Galactic Center, where nucleosynthesis, we believe, is mainly driven by low mass stars.

The sulfur isotopes are produced and destroyed in massive and very massive stars. Their abundances stem from a critical balance between equilibrium and explosive nucleosynthesis. In a $25 M_{\odot}$ star, according to Woosley & Hoffman (1986), ^{34}S is 20 times more efficiently produced at equilibrium than ^{32}S and 100 times more than ^{33}S . In an explosive oxygen burning episode, the three isotopes are produced about evenly. Our $^{32}\text{S}/^{34}\text{S}$ ratio of 10, twice smaller than in the local ISM, could imply that the IMF in the $z = 0.89$ galaxy is different from that of the Milky Way at the same age. Unfortunately, our non-detection of H_2^{33}S brings little information on this respect.

Wang et al. (2004) and Martín et al. (2005) report measurements of the $^{32}\text{S}/^{34}\text{S}$ ratio in the nuclear regions of two starburst galaxies, NGC 4945 and NGC 253. The values they derive (13.5 ± 2.5 and 8 ± 2 , respectively) are similar to that we find in the $z = 0.89$ galaxy. They are much more uncertain, since they rely on the integrated intensity of the broad and weak ^{13}CS line and on the knowledge of the $^{12}\text{C}/^{13}\text{C}$ ratio. In contrast, the $^{32}\text{S}/^{34}\text{S}$ in the LMC (18 ± 6 , according to Chin 1999) is close to that in the local ISM.

5.5. Deuterium

Deuterium is produced in the Big Bang nucleosynthesis with a primordial $[\text{D}/\text{H}]$ ratio of $2.5 \cdot 10^{-5}$ (Spergel et al. 2003). It is completely destroyed in the interior of stars, so that, ignoring infall of unprocessed gas, the D/H ratio is an indicator of the degree of evolution. In the local ISM, the average ratio D/H is $\sim 1.5 \cdot 10^{-5}$.

The deuterium abundance can be greatly enhanced in molecules in the cold and dense gas. Extensive modelling of D-chemistry (see e.g. Roberts & Millar 2000) predicts D/H values as large as 0.01 – 0.1 for molecules embedded in very cold clouds, and such high ratios have been observed in Galactic dark clouds (Guélin et al. 1982), pre-stellar cores (Parise et al. 2002) and in the LMC (Chin et al. 1996).

We searched during 3 hours for the DNC $J = 2 \leftarrow 1$ line with the PdB interferometer; no absorption was detected down to a level of $\tau = 0.011$ (3σ) with a velocity resolution of $\delta V = 4.6 \text{ km s}^{-1}$. Assuming a linewidth similar to the main isotopomer HNC, we obtain an upper limit from the ratio $\text{DNC}(2 \leftarrow 1)/\text{HNC}(2 \leftarrow 1)$: $\text{D}/\text{H} < 0.015$ for the -3 km s^{-1} component.

Our upper limit is less constraining than that derived by Shah et al. (1999) from the double isotopic ratio: $[\text{DCO}^+]/[\text{H}^{13}\text{CO}^+].[^{13}\text{C}/^{12}\text{C}] < 0.0022$. The latter, however, contrary to our result, depends on the knowledge of the C isotopic ratio, a ratio that can be affected by fractionation. Both limits remain far higher than the primordial ratio and tell us little about stellar processing.

6. Molecular column densities

We have argued in §5 that the molecules studied here, which all have a large dipole moment, are likely to be at equilibrium with the cosmic background radiation, whose temperature at $z = 0.89$ is 5.1 K. The observations support this conclusion: Menten et al. (1999) measure a rotation temperature $T_{\text{rot}} = 4.5^{+1.5}_{-0.6}$ K from the observations of two rotational transitions of HC_3N , and WC96

from similar measurements find $T_{\text{rot}} = 4 \pm 2$ for CS, H^{13}CO^+ and N_2H^+ and $T_{\text{rot}} \leq 6$ K for HNC. We therefore assume $T_{\text{ex}} = 5.1$ K in our calculations.

The column densities of Table 8 were calculated from the equation:

$$\mathcal{N} = \frac{8\pi\nu^3}{c^3 A_{ul} g_u} \frac{Q(T_{\text{ex}}) \exp(E_J/T_{\text{ex}})}{(1 - \exp(-h\nu/kT_{\text{ex}}))} \int \tau dV \quad (2)$$

where we assume LTE, optically thin lines and a filling factor of unity. E_J in this equation is the energy of the lower level of the transition, $Q(T_{\text{ex}}) = \sum_{J_i} g_i (2J_i + 1) \exp(-E_{J_i}/kT_{\text{ex}})$ the partition function ($g_i = 3$ for an ortho level, = 1 in any other case), and A_{ul} the Einstein coefficient of the line $A_{ul} = \frac{64\pi^4 \nu^3 \mu^2}{3hc^3} \frac{S_{ul}}{g_u}$. Here, μ is the electric dipole moment, S_{ul} the line strength and g_u the degeneracy factor of the upper level.

As concerns HCO^+ and HCN, whose lines are optically thick, we calculated their column densities by multiplying those of their ^{13}C isotopologues by $^{12}\text{C}/^{13}\text{C} = 27$. This assumes that the $^{12}\text{C}/^{13}\text{C}$ ratio is the same for all molecules and all velocity components. Our results are in good agreement with the values of Menten et al. (1999), which were derived from rotational transitions with lower J and lower opacities.

A crude analysis of the chemistry in the $z = 0.89$ galaxy has been made by WC96 and Menten et al. (1999), who concluded that the molecular abundances in the SW velocity component ($V \approx 0 \text{ km s}^{-1}$) are similar to those of Galactic dark clouds such as TMC 1. The HNC/HCN ratio we find (0.4) is indeed similar to that in those cold clouds (Hirota et al. 1998) and two orders of magnitude larger than in the hot and dense clouds, such as Orion MC-1. A high HNC/HCN ratio probably means that these two species are formed by gas phase ion-molecule reactions via HCNH^+ . Note that a high HNC/HCN ratio has also been reported in the center of nearby starburst galaxies (e.g. Martín et al. 2006).

The $\text{HCO}^+/\text{N}_2\text{H}^+$ ratio, which reflects in the medium dense gas the CO/N_2 ratio, is 6 (adopting the N_2H^+ integrated ($2 \leftarrow 1$) line opacity measured by WC96). Its value is close to the "cosmic" O/N elemental ratio, 7.

Until now, H_2S extragalactic detection was only reported in the LMC (Heikkilä et al. 1999) and NGC 253 (Martín et al. 2005). The abundance of H_2S in the SW component is large (few $\times 10^{-8}$ with respect to H_2 , adopting $\mathcal{N}(\text{H}_2) = 3 \cdot 10^{22} \text{ cm}^{-2}$, WC96), compared to the standard values of $1 - 3 \cdot 10^{-9}$ measured in the quiescent regions of OMC-1 and in the dark clouds (Minh et al. 1989). It is also a factor of ≈ 10 larger than in the local diffuse clouds, as measured by Lucas & Liszt (2002). This overabundance could reflect a large abundance of S in the gas, although the CS abundance seems normal. It could also mean that the absorbing gas at $z = 0.89$ is not that quiescent and that H_2S molecules could be released from dust grains either by intense UV radiation from star forming regions or by shocks generated by young stellar objects, as is observed in the Orion (KL) outflow (Minh et al. 1990). The very wide absorption profile observed in a few pc-large SW absorbing cloud may support this last scenario.

Although we have measured only a few column densities for the NE velocity component ($V = -147 \text{ km s}^{-1}$), those also yield relative abundances similar to those of the cold dark clouds. In particular, the HNC/HCN ratio (0.3) is large.

7. Conclusion

The presence of an intervening nearly face-on spiral galaxy at $z = 0.89$ in the line of sight of the radio loud quasar PKS 1830-211 offers an unique chance to study the chemical and isotopic compositions of the interstellar medium in the spiral arm of a galaxy 2 – 3 times younger than the Milky Way. The use of the PdB interferometer has enabled us to combine very flat baselines and high sensitivity, making it possible to measure reliably the C, N, O and S isotopic abundance ratios in HCO^+ , HCN , HNC , CS , and H_2S . The ratios derived from different species or velocity components are fully consistent, which supports the view that they are not affected by residual opacity effects and/or fractionation effects and that they reflect the elemental isotopic ratios.

A comparison of the isotopic ratios in the $z = 0.89$ galaxy with those observed in the local ISM, the Galactic Center, the circumstellar envelope IRC+10216 and the Solar System shows major differences with these sources. Mainly, the $^{17}\text{O}/^{18}\text{O}$, and $^{14}\text{N}/^{15}\text{N}$ ratios, which are sensitive probes of the degree of processing of the gas by low mass stars and which are expected to increase with time are found to be smaller than in the ISM or the Solar System and much smaller than in the Galactic Center and in the fully processed low-mass star envelope IRC+10216. Most remarkably, the observed $^{16}\text{O}/^{18}\text{O}$ ratio is a factor of 10 lower than in the ISM and the Solar System and the $^{32}\text{S}/^{34}\text{S}$ ratio is twice lower than in the Galactic sources. These latter ratios result mainly from nucleosynthesis in high mass stars, it is likely that the stellar Initial Mass Function in the $z = 0.89$ galaxy is different from that of the Milky Way at the same age. The low $^{17}\text{O}/^{18}\text{O}$, and $^{14}\text{N}/^{15}\text{N}$ ratios are consistent with the young age of the galaxy (< 6 Gyr) which is smaller than the lifetime of stars with masses $< 1.5 M_{\odot}$ and severely limits the importance of low mass stars in the regeneration of the ISM.

The isotopic ratios observed towards PKS 1830-211, although more extreme, are not unisimilar to those derived in the starburst nuclei of nearby galaxies, such as NGC 253, M82 and NGC 4945 (see e.g. Martín et al. 2006). The later ratios, which result from the observation of weak and broad emission lines, are however far more uncertain.

The extension of this study to other remote galaxies is hampered by the small number of millimeter radio sources whose line-of-sight intercepts the plane of a remote galaxy. PKS 1830-211 is by far the brightest such source. The second best, at present, is the gravitational lens B0218+357 and several molecular lines have been observed in absorption at $z = 0.68$ toward this object (Wiklind & Combes 1995, Menten & Reid 1996, Combes & Wiklind 1997). Even in this object, the detection of less abundant species is difficult (Henkel et al. 2005). Fortunately, the flux of this source has been growing lately at millimeter wavelengths, giving hope that the rare carbon, oxygen and sulfur isotopes can be studied in the near future.

Acknowledgements. We would like to thank all the members of the IRAM staff from the Plateau de Bure who made these observations possible. S.M. thanks Dr. Y.C. Minh for fruitful and stimulating discussions. We wish to thank the referee, whose comments helped to improve the paper. Based on observations carried out with the IRAM Plateau de Bure Interferometer. IRAM is supported by INSU / CNRS (France), MPG (Germany) and IGN (Spain).

References

Anders E. & Grevesse N. 1989, *Geochim. Cosmochim. Acta*, 53, 197
 Bensch F., Pak I., Wouterloot J.G.A., Klapper G. & Winnemisser G. 2001, *ApJ*, 562, L185
 Carilli C.L., Menten K.M., Reid M.J. et al. 1998, *astro-ph/9801157*
 Cernicharo J., Guélin M. & Kahane C. 2000, *A&AS*, 142, 181

Chengalur J.N., De Bruyn A.G. & Narasimha D. 1999, *A&A*, 343, 79
 Chin Y.-N., Henkel C., Whiteoak J.B. et al. 1996, *A&A*, 305, 960
 Chin Y.-N. 1999, *IAU Symp. Vol. 190*, p.279, Eds. Chu Y.H. et al.
 Chin Y.-N., Henkel C., Langer N. & Mauersberger R. 1999, *ApJ*, 512, L143
 Combes F. & Wiklind T. 1995, *A&A*, 303, L61
 Combes F. & Wiklind T. 1997, *ApJ*, 486, L79
 Combes F. & Wiklind T. 1998, *ESO Messenger*, 91, 29
 Combes F. 1999, *Ap&SS*, 269, 405
 Frerking M.A., Wilson R.W., Linke R.A. & Wannier P.G. 1980, *ApJ*, 240, 65
 Frye B., Welch W.J. & Broadhurst T. 1997, *ApJ*, 478, 25
 Gérin M., Philipps T.G., Benford D.J. et al. 1997, *ApJ*, 488, 31
 Guélin M., Langer W.D. & Wilson R.W. 1982, *A&A*, 107, 107
 Harrison A., Henkel C. & Russell A. 1999, *MNRAS*, 303, 157
 Heikkilä A., Johansson L.E.B. & Olofsson H. 1999, *A&A*, 344, 817
 Henkel C. & Mauersberger R. 1993, *A&A*, 274, 730
 Henkel C., Chin Y., Mauersberger R. & Whiteoak J.B. 1998, *A&A*, 329, 443
 Henkel C., Jethava N., Kraus A. et al. 2005, *A&A*, 440, 893
 Hirota T., Yamamoto S., Mikami H. & Ohishi M. 1998, *ApJ*, 503, 717
 Jauncey D.L., Reynolds J.E., Tzioumis A.K. et al. 1991, *Nature*, 352, 132
 Kahane C., Gomez-Gonzalez J., Cernicharo J. & Guélin M. 1988, *A&A*, 190, 167
 Kahane C., Cernicharo J., Gomez-Gonzalez J. & Guélin M. 1992, *A&A*, 256, 235
 Koopmans L.V.E. & de Bruyn A.G. 2005, *MNRAS*, 360, L6
 Landré V., Prantzos N., Aguer P. et al. 1990, *A&A*, 240, 85
 Langer W.D., Graedel T.E., Frerking M.A. & Armentrout P.B. 1984, *ApJ*, 277, 581
 Lidman C., Courbin F., Meylan G. et al. 1999, *ApJ*, 514, 57
 Lovell J.E.J., Reynolds J.E., Jauncey D.L. et al. 1996, *ApJ*, 472, L5
 Lovell J.E.J., Jauncey D.L., Reynolds J.E. et al. 1998, *ApJ*, 508, L51
 Lucas R. & Liszt H. 1996, *A&A*, 307, 237
 Lucas R. & Liszt H. 1998, *A&A*, 337, 246
 Lucas R. & Liszt H. 2002, *A&A*, 384, 1054
 Martín S., Martín-Pintado J., Mauersberger R., Henkel C. & García-Burillo S. 2005, *ApJ*, 620, 210
 Martín S., Mauersberger R., Martín-Pintado J., Henkel C. & García-Burillo S. 2006, *ApJS*, 164, 450
 Menten K.M. & Reid M.J. 1996, *ApJ*, 465, L99
 Menten K.M., Carilli C.L., Reid M.J. 1999, *ASP Conf. Ser.*, 156, 218
 Milam S.N., Savage C., Brewster M.A., Ziurys L.M. & Wyckoff S. 2005, *ApJ*, 634, 1126
 Minh Y.C., Irvine W.M. & Ziurys L.M. 1989, *ApJ*, 345, L63
 Minh Y.C., Ziurys L.M., Irvine W.M. & McGonagle D. 1990, *ApJ*, 360, 136
 Muller S. & Guélin M. 2003, *ASP Conf. Ser.*, 304, 252
 Nair S., Narasimha D. & Rao A.P. 1993, *ApJ*, 407, 46
 Parise B., Ceccarelli C., Tielens A.G.G.M et al. 2002, *A&A*, 393, 49
 Patnaik A. et al. 1994, in *Proceedings of the 1993 Liege Symposium on Gravitational Lensing*
 Penzias A.A. 1980, *Science*, 208, 663
 Penzias A.A. 1981, *ApJ*, 249, 518
 Polehampton E.T., Baluteau J.-P. & Swinyard B.M. 2005, *A&A*, 437, 957
 Prantzos N., Aubert O. & Audouze J. 1996, *A&A*, 309, 760
 Roberts H. & Millar T.J. 2000, *A&A*, 361, 388
 Sage L.J., Mauersberger R. & Henkel C. 1991, *A&A*, 249, 31
 Shah R.Y., Wootten A., Mangum J.G., Carilli C.L. & Menten K.M. 1999, *ASP Conf. Ser.*, 156, 233
 Spergel D.N., Verde L., Peiris H.V. et al. 2003, *ApJS*, 148, 175
 Subrahmanyan R., Narasimha D., Pramesh Rao A. & Swarup G. 1990, *MNRAS*, 246, 263
 Swift J.J., Welch W.J. & Frye B.L. 2001, *ApJ*, 549, L29
 van Ommen T.D., Jones D.L., Preston R.A. & Jauncey D.L. 1995, *ApJ*, 444, 516
 Wang M., Henkel C., Chin Y.N. et al. 2004, *A&A*, 422, 883
 Wiklind T. & Combes F. 1994, *A&A*, 286, L12
 Wiklind T. & Combes F. 1995, *A&A*, 299, 382
 Wiklind T. & Combes F. 1996, *Nature*, 379, 139 (**WC96**)
 Wiklind T. & Combes F. 1998, *ApJ*, 500, 129 (**WC98**)
 Wiklind T. & Combes F. 1999, *astro-ph/9909314*
 Wilson T. & Matteucci F. 1992, *A&A Rev.*, 4, 1
 Wilson T.L. & Rood R.T. 1994, *ARA&A*, 32, 191
 Winn J.N., Kochanek C.S., McLeod B.A. et al. 2002, *ApJ*, 575, 103
 Woosley S.E. & Hoffman R. 1986, in "Nucleosynthesis and Stellar Evolution", eds Hauck B., Maeder A. & Meynet G., Geneva Observatory, p.67
 Wouterloot J.G.A., Brand J. & Henkel C. 2005, *A&A*, 430, 549

List of Objects

‘PKS 1830-211’ on page 1

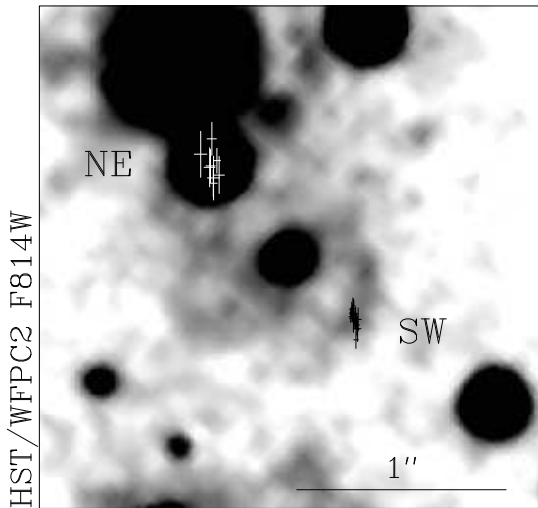
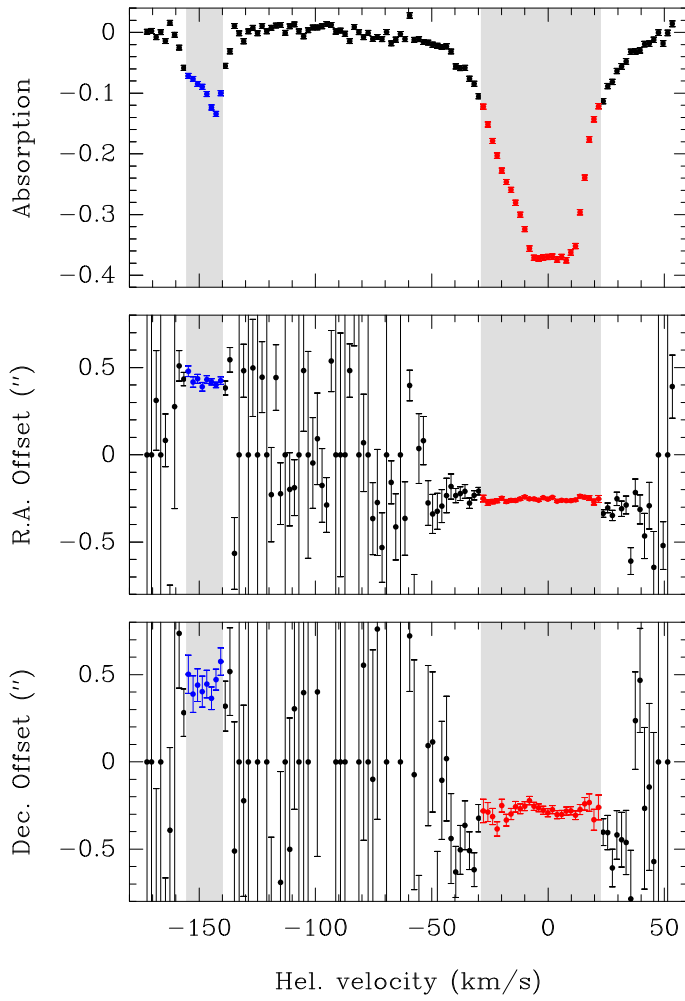


Fig. 1. Positions of the SW and NE absorption components as observed with PdBI in the HCO^+ ($2 \leftarrow 1$) line. The R.A. and Dec. offsets (top) at each velocity channels, indicating the position of the absorption (shaded area), were obtained from a fit of the interferometric visibilities. These positions are reported on a Hubble Space Telescope I band image of the $z = 0.89$ galaxy (bottom). The HST data were retrieved from the STScI Archive site: "<http://archive.stsci.edu/hst/search.php>" and reduced within IRAF. The SW absorption clearly falls right on top of a spiral arm.

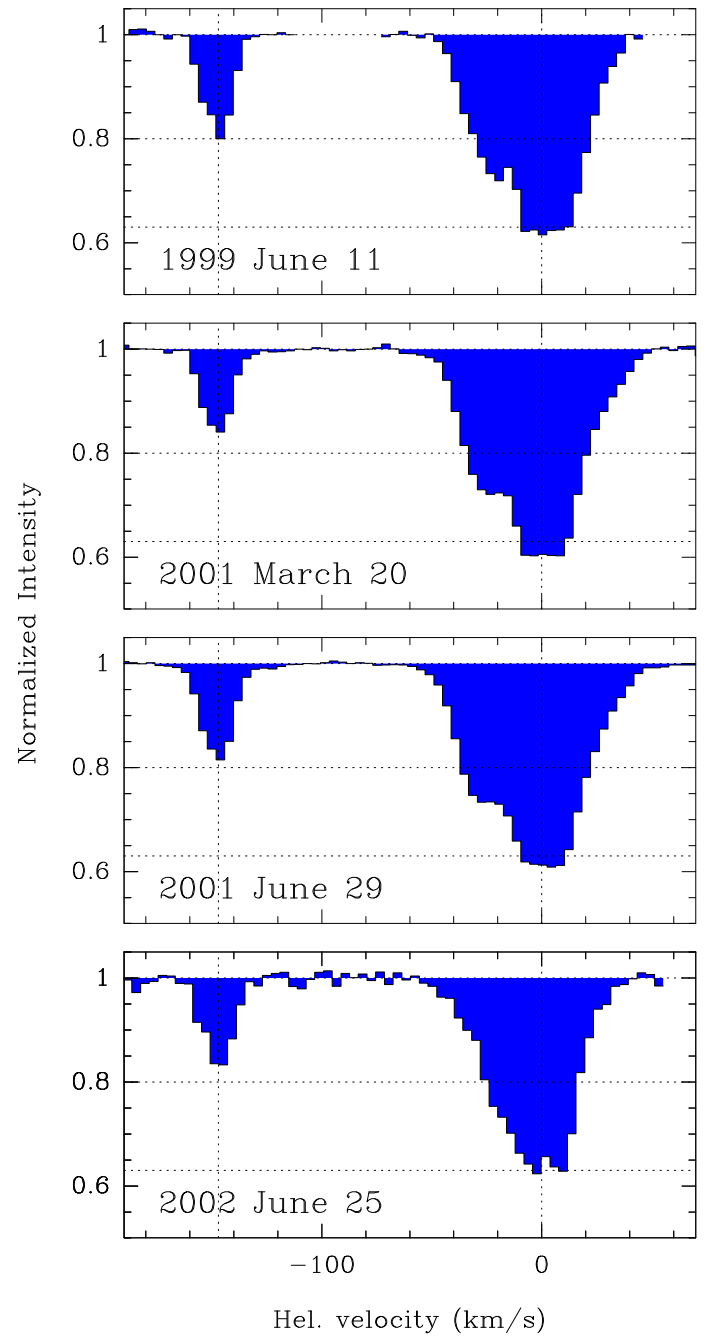


Fig. 2. HCO^+ absorption lines observed at different epochs from 1999 to 2002. For comparison, all spectra have been smoothed to the same spectral resolution of 1.25 MHz ($\approx 4 \text{ km s}^{-1}$).

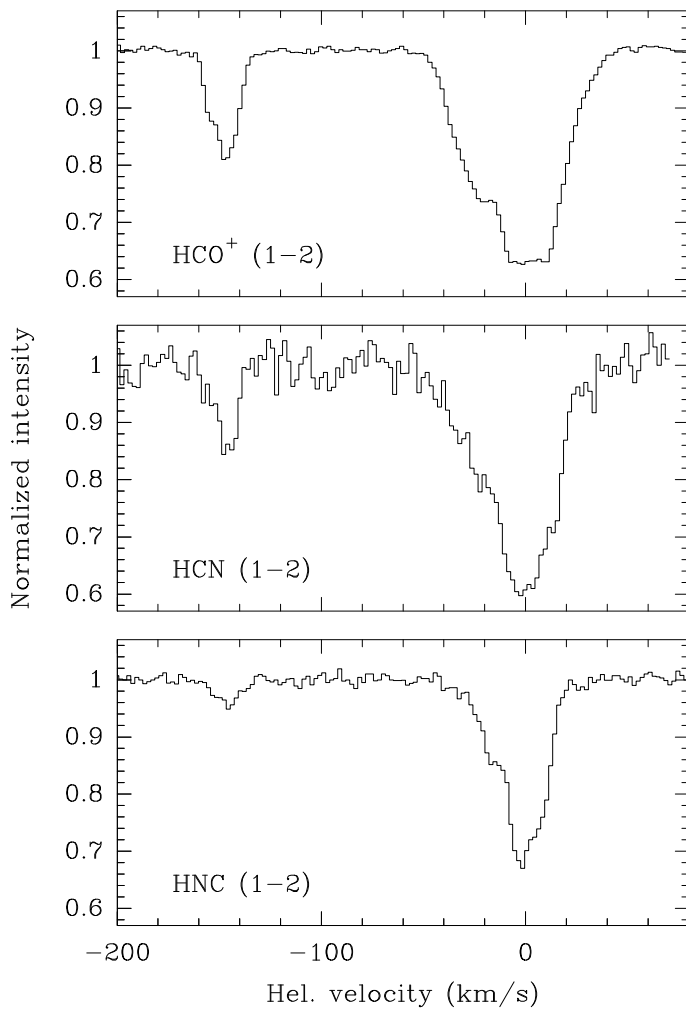


Fig. 3. Spectra of the main isotopomers of HCO^+ , HCN and HNC (from top to bottom respectively). The velocity resolution is 2 km s^{-1} .

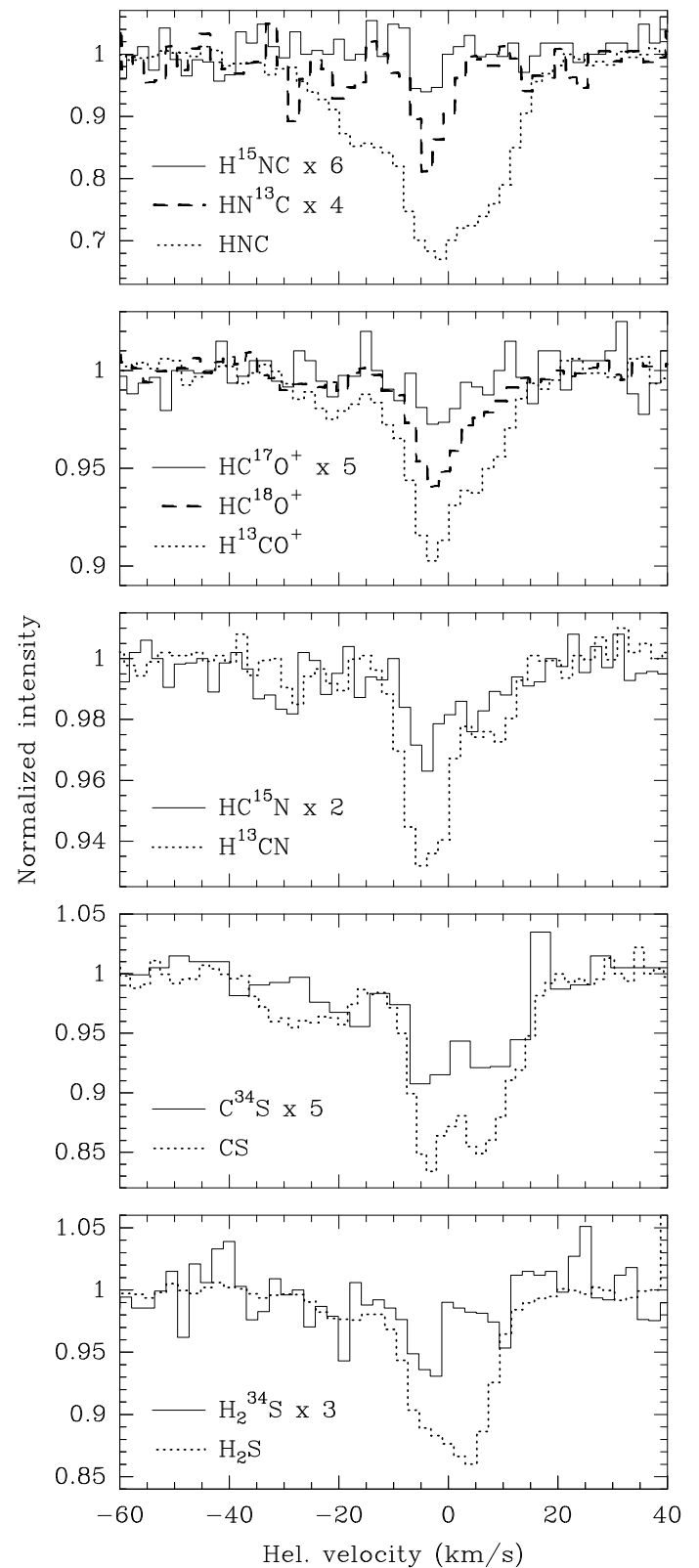


Fig. 4. Spectra of the different species and isotopomers observed for this survey. From top to bottom: HNC , HCO^+ , HCN , CS and H_2S isotopomers. For a better comparison, the weak isotopomers are scaled and renormalized, with scaling factor indicated in each box. The velocity resolution is $\approx 2 \text{ km s}^{-1}$ except for the C^{34}S spectrum, for which it is $\approx 4 \text{ km s}^{-1}$.

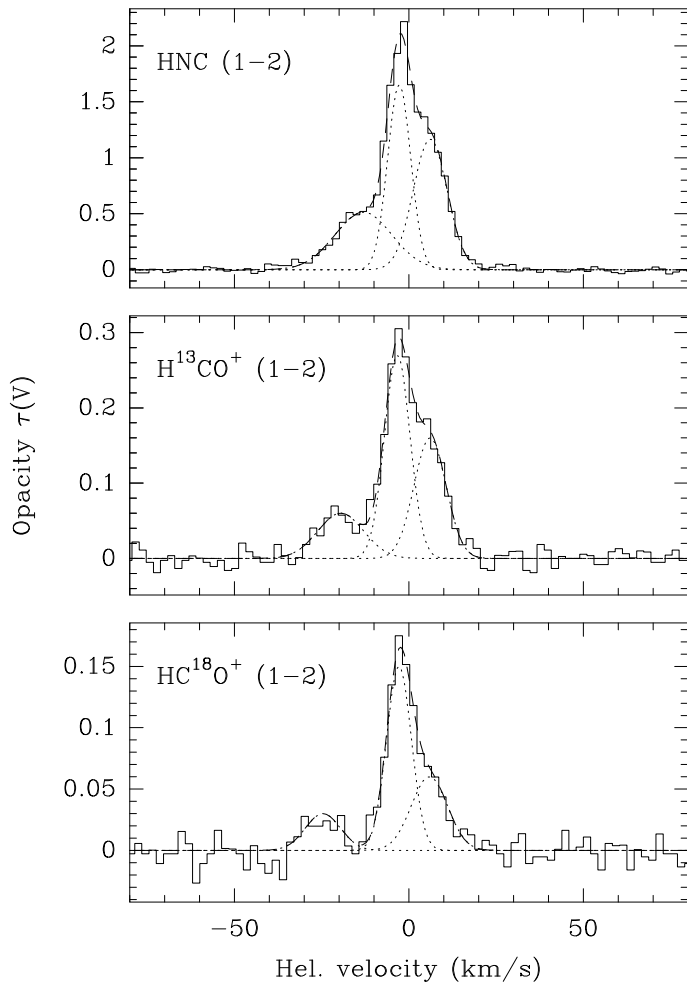


Fig. 5. Line opacity profiles of the $J=2 \leftarrow 1$ HNC (up), $H^{13}CO^+$ (middle) and $HC^{18}O^+$ (down) for the SW component with the decomposition into Gaussian components. Note the similarity of the profiles in spite of the large difference in opacity.

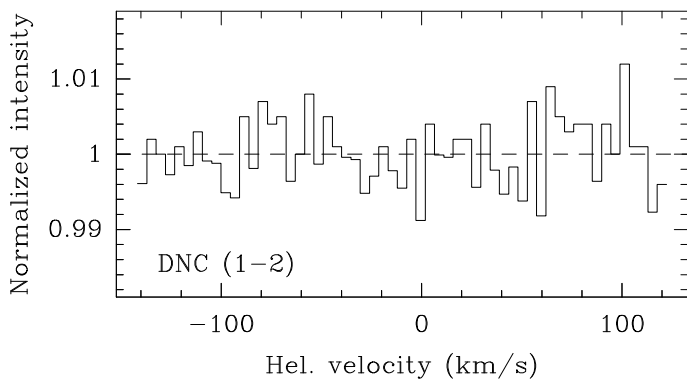


Fig. 6. Spectrum observed at the frequency of the DNC ($2 \leftarrow 1$) line, smoothed to a resolution of 4.6 km s^{-1} . The RF was calibrated on the quasar 3C454.3. No further baseline has been removed, except for a constant offset. Note the quality of the baseline resulting from interferometric observations. The narrow negative feature at 0 km s^{-1} is not significant.

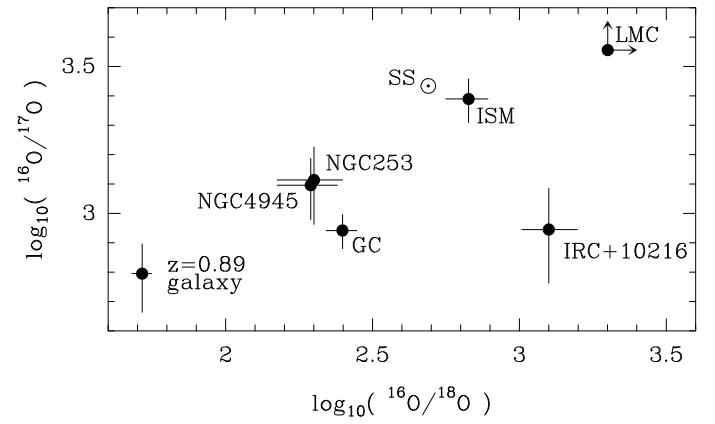


Fig. 7. Oxygen isotopic ratios diagram $^{16}O/^{17}O$ vs $^{16}O/^{18}O$ for different sources: the Solar System (SS), the Large Magellanic Cloud (LMC), the local interstellar medium (ISM), the AGB star IRC+10216, the Galactic center (GC), 2 nuclei of nearby starbursts (NGC 253 and NGC 4945) and the $z = 0.89$ galaxy. The values and references are listed in Table 7.

Online Material

Table 2. Observational data.

Line	Redshifted frequency † (MHz)	Date	Time ON source	Array [◊]
HCO ⁺ (2 ← 1)	94587.58	1999/06/11	3.0 h	4C1
		2001/03/20	2.5 h	4ANT
		2001/06/29	3.5 h	4ANT
		2002/06/25	3.0 h	5D
		2003/02/26	2.2 h	6Ap
		2003/03/01	2.6 h	6Ap
H ¹³ CO ⁺ (2 ← 1)	92006.01	1999/06/13	2.9 h	4C1
		2002/06/21	2.7 h	5D
		2002/06/23	3.7 h	5D
		2002/07/15	1.3 h	5D
HC ¹⁸ O ⁺ (2 ← 1)	90317.61	1999/08/03	3.2 h	4ANT
		1999/09/09	2.8 h	4C2
		1999/10/02	2.8 h	4C2
		1999/11/12	1.8 h	5D
		2001/05/08	1.7 h	4ANT
HC ¹⁷ O ⁺ (2 ← 1)	92327.67	1999/07/08	4.3 h	4D2
		1999/07/15	3.7 h	4D2
		1999/07/25	3.0 h	4D2
		1999/09/24	2.0 h	4C2
		1999/10/14	2.3 h	4B1
		1999/10/26	2.0 h	4B1
		1999/10/29	3.2 h	4D1
		1999/11/01	3.2 h	4D1
		1999/11/08	1.7 h	5D
		HCN (2 ← 1)	93996.83	1999/08/04
2003/08/03	1.3 h			30M
H ¹³ CN (2 ← 1)	91566.38	1999/08/29	2.7 h	5D
		2001/07/03	2.6 h	5D
HC ¹⁵ N (2 ← 1)	91264.34	1999/08/25	4.2 h	4D1
		1999/10/04	1.6 h	4C2
		2001/05/28	2.0 h	4ANT
		2001/05/30	1.5 h	4ANT
		2001/08/13	3.3 h	4D1
		2001/08/14	2.8 h	4D1
		2001/08/15	3.7 h	4D1
HNC (2 ← 1)	96151.68	2002/08/07	3.7 h	5D
HN ¹³ C (2 ← 1)	92362.69	2001/08/26	2.7 h	4D1
		2001/10/15	1.2 h	4ANT
H ¹⁵ NC (2 ← 1)	94244.99	2001/08/04	2.8 h	4D1
		2001/08/07	3.3 h	4D1
		2001/08/25	2.7 h	4D1
DNC (2 ← 1)	80924.89	2001/08/28	2.7 h	4D1
CS (4 ← 3)	103909.33	1999/07/09	3.3 h	4D2
C ³⁴ S (4 ← 3)	102246.49	1999/09/21	1.8 h	4C2
		1999/09/23	2.2 h	4C2
		2001/05/09	1.8 h	3ANT
		2001/05/10	3.4 h	5D
		2001/05/14	2.6 h	5D
H ₂ S (1 ₁₀ ← 1 ₀₁) [‡]	89490.39	2005/07/05	4.3 h	5D
		2005/07/29	3.2 h	5D
		2005/09/05	3.0 h	5D
		2005/09/09	1.8 h	5D

Notes:

[◊] The number of antennae is given with the name of the array configuration if defined.[†] Redshifted frequencies are given for $z = 0.88582$.[‡] The H₂³⁴S (1₁₀ ← 1₀₁) (89038.47 MHz) and H₂³³S (1₁₀-1₀₁) (89256.88 MHz) were observed simultaneously in the same correlator setup.

Table 4. Results of the decomposition of the SW opacity profiles into multiple Gaussian components.

SW	$V \simeq -3 \text{ kms}^{-1}$				$V \simeq 7 \text{ kms}^{-1}$				$V \simeq -23 \text{ kms}^{-1}$			
	V_0 (kms^{-1})	τ	$\Delta V_{1/2}$ (kms^{-1})	$\int \tau dV$ (kms^{-1})	V_0	τ	$\Delta V_{1/2}$ (kms^{-1})	$\int \tau dV$ (kms^{-1})	V_0	τ	$\Delta V_{1/2}$ (kms^{-1})	$\int \tau dV$ (kms^{-1})
H^{13}CO^+ (1-2)	-3.3	0.27	8.6	2.5 (0.05)	6.1	0.16	10.8	1.8 (0.06)	-19.5	0.06	15.5	1.0 (0.07)
HC^{18}O^+ (1-2)	-2.8	0.15	8.4	1.4 (0.06)	5.9	0.06	12.2	0.7 (0.07)	-24.6	0.03	11.8	0.3 (0.07)
HC^{17}O^+ (1-2)	-1.8	0.01	10.0	0.15 (0.03)	-	-	-	-	-	-	-	-
H^{13}CN (1-2)	-3.8	0.21	9.2	2.1 (0.08)	8.4	0.08	7.6	0.6 (0.07)	-25.6	0.03	11.0	0.3 (0.08)
HC^{15}N (1-2)	-3.0 [†]	0.04	7.4	0.31 (0.03)	7.0 [†]	0.02	10.0	0.23 (0.04)	-	-	-	-
HNC (1-2)	-2.7	1.65	7.8	13.7 (0.07)	6.1	1.17	11.5	14.2 (0.08)	-13.0	0.51	19.3	10.5 (0.1)
HN^{13}C (1-2)	-3.3	0.12	6.8	0.9 (0.07)	-	-	-	-	-	-	-	-
H^{15}NC (1-2)	-	(0.014)	-	≤ 0.17	-	-	-	-	-	-	-	-
DNC (1-2)	-	(0.011)	-	≤ 0.19	-	-	-	-	-	-	-	-
CS (3-4)	-3.1	0.54	8.3	4.8 (0.08)	7.4	0.50	9.8	5.2 (0.09)	-25.5	0.13	16.3	2.3 (0.1)
C^{34}S (3-4)	-3.5	0.06	7.4	0.44 (0.04)	7.9	0.05	9.3	0.49 (0.05)	-18.1	0.02	10.1	0.25 (0.05)
H_2S ($1_{01}-1_{10}$)	-6.6	0.29	6.3	2.0 (0.05)	2.0	0.48	9.5	4.9 (0.06)	-19.4	0.07	11.1	0.8 (0.07)
H_2^{34}S ($1_{01}-1_{10}$)	-4.3	0.06	7.2	0.49 (0.07)	-	-	-	-	-	-	-	-
H_2^{33}S ($1_{01}-1_{10}$)	-	(0.016)	-	≤ 0.19	-	-	-	-	-	-	-	-

Notes: Uncertainties on the integrated opacity are estimated as $\sigma_\tau \sqrt{\delta V \Delta V_{1/2}}$ where σ_τ is the rms uncertainty on the opacity for the velocity resolution δV ($\simeq 2 \text{ kms}^{-1}$ here). Upper limits are calculated as $3\sigma_\tau \sqrt{\Delta V_{1/2} \delta V}$ where $\Delta V_{1/2}$ is taken as the velocity width of the same component of the main isomer or isotopomer. The quoted uncertainties reflect the statistical noise and baseline residuals, but not the uncertainties on the magnification ratio \mathfrak{R} , which is assumed to remain constant.

[†] Fixed parameter.

Table 7. Comparison of the C, N, O and S isotopic ratios in the $z = 0.89$ galaxy (SW absorption) with different other environments.

	$^{12}\text{C}/^{13}\text{C}$	$^{14}\text{N}/^{15}\text{N}$	$^{16}\text{O}/^{18}\text{O}$	$^{18}\text{O}/^{17}\text{O}$	$^{32}\text{S}/^{34}\text{S}$
$z = 0.89$ galaxy	27 ± 2	130^{+20}_{-15}[†]	52 ± 4[†]	12^{+3}_{-2}	10 ± 1
Solar System (a)	89	270	490	5.5	22
Local ISM (b)	59 ± 2	237^{+27}_{-21}	672 ± 110	3.65 ± 0.15	19 ± 8
Galactic Center (c)	25 ± 5	900 ± 200	250 ± 30	3.5 ± 0.2	18 ± 5
IRC+10216 (d)	45 ± 3	> 4400	1260^{+315}_{-240}	0.7 ± 0.2	21.8 ± 2.6
LMC (e)	62 ± 5	114 ± 14	> 2000	1.8 ± 0.4	18 ± 6
NGC 253 (f)	40 ± 10	-	200 ± 50	6.5 ± 1	8 ± 2
NGC 4945 (g)	50 ± 10	105 ± 25	195 ± 45	6.4 ± 0.3	13.5 ± 2.5

[†] Derived from a double ratio assuming $^{12}\text{C}/^{13}\text{C} = 27 \pm 2$.

References: a) Anders & Grevesse 1989; b) Lucas & Liszt 1998, except for $^{18}\text{O}/^{17}\text{O}$ taken from Penzias 1981; c) Wilson & Matteucci 1992, Wilson & Rood 1994 and references therein; d) Kahane et al. 1988, 1992 and Cernicharo et al. 2000; e) Chin 1999; f) Henkel & Mauersberger 1993, Harrison et al. 1999 and Martín et al. 2005; g) Wang et al. 2004.

Table 8. Total molecular column densities towards the SW and NE absorption.

	μ (Debye)	S_{ul}	g_u	A_{ul} (10^{-4} s^{-1})	$E_{J,low}$ (K)	Q(5.14 K)	\mathcal{N}_{SW} (10^{12} cm^{-2})	\mathcal{N}_{NE} (10^{12} cm^{-2})
HCO ⁺	3.90	2	5	4.02	4.3	2.77	300 (23) [†]	11.4 (0.1)
H ¹³ CO ⁺	3.90	2	5	3.70	4.2	2.83	11.1 (0.2)	≤ 0.25
HC ¹⁸ O ⁺	3.90	2	5	3.50	4.1	2.88	5.1 (0.3)	–
HC ¹⁷ O ⁺							0.4 (0.1) [†]	–
HCN	2.99	2	5	2.32	4.3	2.78	289 (25) [†]	12.3 (0.7)
H ¹³ CN	2.99	2	5	2.14	4.1	2.84	10.7 (0.5)	≤ 0.5
HC ¹⁵ N	2.99	2	5	2.13	4.1	2.85	2.1 (0.1)	–
HNC	3.05	2	5	2.58	4.4	2.73	129.0 (0.5)	3.7 (0.2)
HN ¹³ C							4.8 (0.4) [†]	–
H ¹⁵ NC							1.0 (0.2) [†]	–
DNC	3.05	2	5	1.54	3.7	3.17	≤ 0.7	–
CS	1.96	4	9	1.50	14.1	4.72	560 (7)	13 (4)
C ³⁴ S	1.96	4	9	1.42	13.9	4.79	53 (4)	–
H ₂ S	0.97	4.5	9	0.26	19.8	1.28	1104 (15)	≤ 17
H ₂ ³⁴ S							110 (11) [†]	–

Notes: The column densities marked with [†] were estimated using the value of a nearby isotopomer, corrected from the corresponding isotopic ratio. Upper limits on column densities are calculated from the 3σ upper limits on the integrated opacities in Table 4 and Table 5.